Available online at www.sciencedirect.com

ScienceDirect

Advances in Space Research 71 (2023) 268–274

ADVANCES IN SPACE RESEARCH (a COSPAR publication)

www.elsevier.com/locate/asr

A comparative study on geoeffective and non-geoeffective corotating interaction regions

Jibin V. Sunny [a], Archana Giri Nair [b], Megha Babu [b], Rajkumar Hajra [a,*]

[a] Indian Institute of Technology Indore, Indore, Madhya Pradesh 453552, India

[b] Department of Sciences, Amrita School of Engineering, Amrita Vishwa Vidyapeetham, Amritanagar, Coimbatore, Tamil Nadu 641112, India

Received 13 June 2022; received in revised form 19 September 2022; accepted 22 September 2022
Available online 28 September 2022

Abstract

A long database of corotating interaction regions (CIRs) is used to investigate their geoeffectiveness. Among 290 CIR events identified during Solar Cycle 24 (2008–2019), 88 (30%) are found to be geoeffective in causing geomagnetic storms with the symmetric ring current index [SYM-H] peak $\leqslant -50$ nT, and 202 (70%) are non-geoeffective with the minimum SYM-H > -50 nT. Based on a comparative study of the geoeffective and non-geoeffective CIRs, following results are obtained. Geoeffective and non-geoeffective CIRs have comparable duration (28 ± 15 hours, 26 ± 14 hours, respectively) and radial extent (0.33 ± 0.17 AU, 0.30 ± 0.17 AU, respectively), on average. While the mean solar-wind plasma speed during the geoeffective (503 ± 70 km s^{-1}) and non-geoeffective (491 ± 63 km s^{-1}) CIRs exhibits no statistical difference, the geoeffective CIRs have $\approx 25\%$ higher peak plasma density, $\approx 45\%$ higher ram pressure, $\approx 42\%$ higher temperature, $\approx 39\%$ higher interplanetary magnetic field (IMF) magnitude, $\approx 57\%$ stronger IMF southward component, and $\approx 61\%$ stronger reconnection electric field than the non-geoeffective events, on average. The auroral electrojet index [AE] and SYM-H are found to be, respectively, $\approx 58\%$ and $\approx 192\%$ stronger during the geoeffective CIRs than the non-geoeffective events. The typical characteristic solar-wind and geomagnetic activity parameters given in this article can be useful for space weather modeling and prediction purposes.

Keywords: Coronal holes; Interplanetary magnetic fields; Geomagnetic disturbances; Solar cycle; Solar wind

1. Introduction

Space weather events originate on the Sun, and can impact the solar system bodies such as planets and comets (Echer et al., 2005; Cannon et al., 2013; Hajra et al., 2018, 2020, 2021; Lakhina et al., 2020; Tsurutani et al., 2020; Franco et al., 2021; Tsurutani and Hajra, 2021; Hajra, 2022a,b, and references therein). Corotating interaction region (CIR) is one such event. CIR results from the interaction between a slow solar-wind and a high-speed stream (HSS) emanated from a solar coronal hole (Belcher and Davis, 1971; Siscoe, 1972; Smith and Wolfe, 1976; Pizzo, 1978; Tsurutani et al., 1995).

Near-Earth CIRs are characterized by compressed (high) plasma density [N_{sw}] and interplanetary magnetic field (IMF) magnitude [B_0], and highly fluctuating IMF components (Alves et al., 2006; Jian et al., 2006; Jian et al., 2019; Hajra and Sunny, 2022; Hajra et al., 2022, and references therein). The IMF southward component can reconnect with dayside magnetopause geomagnetic field (northward) resulting in an enhanced solar-wind kinetic energy transfer into the Earth's magnetosphere (Dungey, 1961; Tsurutani and Gonzalez, 1987). This leads to an increase in the ring current flow encircling the Earth's magnetic equator (Frank, 1967; Williams, 1987; Daglis et al., 1999). The southward magnetic field induction on

* Corresponding author.
E-mail address: rajkumarhajra@yahoo.co.in (R. Hajra).

https://doi.org/10.1016/j.asr.2022.09.051
0273-1177/

the Earth's surface due to the enhanced (westward) ring current causes a resultant geomagnetic field reduction, commonly known as the geomagnetic storm (Chapman and Bartels, 1940; Gonzalez et al., 1994). Earlier studies have shown that ≈ 25–33% of the CIRs are geoeffective in causing geomagnetic storms with the peak (minimum) ring current index [SYM-H] ⩽ −50 nT (Alves et al., 2006; Alves et al., 2011; Verbanac et al., 2011; Chi et al., 2018; Hajra and Sunny, 2022). It is important to explore the factors responsible for the CIR geoeffectiveness. Why are some CIRs geoeffective and some are not? While a large volume of work has been done on the CIR variations (Richardson et al., 2000; Alves et al., 2006; Jian et al., 2006; Tsurutani et al., 2006; Jian et al., 2019), their characteristics (Alves et al., 2006; Jian et al., 2006; Jian et al., 2019), and their geoeffectiveness (see Tsurutani and Gonzalez, 1987; Alves et al., 2006; Alves et al., 2011; Zhang et al., 2008; Lei et al., 2011; Verbanac et al., 2011; Gardner et al., 2012; Hajra et al., 2013, 2017, 2022; Tsurutani et al., 2016a,b; Chi et al., 2018; Hajra and Tsurutani, 2018, and references therein), there has been no comparative study between the geoeffective and non-geoeffective CIR events, to our knowledge.

The aim of this present work is to conduct a comparative analysis of the solar-wind and interplanetary features, and geomagnetic activity during geoeffective and non-geoeffective CIR events. For this study, we will use the CIR database developed by Hajra and Sunny (2022) for the period from January 2008 through December 2019 (Solar Cycle 24). This comparative study may be important for identifying the factors controlling the geoeffectiveness of space weather events in general.

2. Data and methods

The one-minute resolution solar-wind plasma and IMF data analyzed in this work are collected from NASA's OMNIWeb (https://omniweb.gsfc.nasa.gov/), where the solar-wind observations made by several spacecraft upstream of Earth are shifted in time to take into account the arrival time of the solar wind to the Earth's bow-shock nose. The geomagnetic condition is explored by the auroral electrojet index [AE] (Davis and Sugiura, 1966) and the ring current index [SYM-H] (Wanliss and Showalter, 2006; Iyemori et al., 2010). The geomagnetic indices (one-minute) are obtained from the World Data Center for Geomagnetism, Kyoto, Japan (https://wdc.kugi.kyoto-u.ac.jp/).

For the CIR events studied in this work, start and end times are obtained from the Electronic Supplementary Material available at https://doi.org/10.1007/s11207-022-01962-1 (Hajra and Sunny, 2022). A CIR is identified as a region of the compressed (high) plasma density [N_{sw}] and IMF magnitude [B_0] between a slow-speed stream (SSS) and an HSS emanated from a solar coronal hole (Smith and Wolfe, 1976). For a detailed description of the method of the CIR identification, and a discussion on the associated uncertainty, we refer the reader to Hajra and Sunny (2022).

The CIR events are characterized by the solar-wind plasma and IMF parameters, namely, the mean solar-wind speed [V_{sw}], the maximum plasma density [N_{sw}], ram pressure [P_{sw}], temperature [T_{sw}], IMF B_0, the minimum value of the IMF B_z component or the maximum B_s, and the maximum electric field [E_{sw}]. B_s is the southward component of IMF, defined as $-B_z$ for $B_z < 0$. E_{sw} is the dawn-dusk component [E_y] of the solar-wind electric field vector. The reconnection electric field [VB_s] is defined as E_{sw} for $B_z < 0$. The latter has been shown to be the main driver of geomagnetic activity (e.g. Burton et al., 1975; Tsurutani et al., 1992; Finch et al., 2008; Hajra, 2021). As the CIRs represent compressed plasma and magnetic fields, such a characterization is suitable, and has been done in earlier works (e.g. Alves et al., 2006; Jian et al., 2006, 2019, and references therein). We also estimated their duration from start to end. During the CIR intervals, we computed their radial extent using the solar-wind plasma radial velocity component [V_x]. We use here the geocentric solar magnetospheric (GSM) coordinates, where the x-axis is directed towards the Sun and the y-axis is in the $\mathbf{\Omega} \times \hat{x}/|\mathbf{\Omega} \times \hat{x}|$ direction, $\mathbf{\Omega}$ is aligned with the magnetic south-pole axis of the Earth. The z-axis completes a right-hand system. In GSM system, V_x is negative (outward from the Sun). Thus, the CIR radial extent is computed as the area under the $|V_x|$ curve.

To characterize the geomagnetic activity associated with the CIRs, we estimated the maximum and minimum values of the AE and SYM-H indices, respectively during each of the CIR intervals. Following Gonzalez et al. (1994), if the minimum SYM-H is less than or equal to −50 nT during a CIR interval, the CIR is classified as a "geoeffective CIR", and if the minimum SYM-H is greater than −50 nT during a CIR interval, it is classified as a "non-geoeffective CIR".

3. Results and discussion

3.1. Geoeffective and non-geoeffective CIR events: Case Studies

Fig. 1 shows three CIR events occurring during 2013. Solar-wind plasma $V_{sw}, V_x, N_{sw}, T_{sw}$, IMF B_0, and B_x-, B_y-, B_z- components, and E_{sw} are explored to study the solar-wind and interplanetary condition during the CIRs. From enhanced B_0 and N_{sw}, three CIRs are identified from ≈ 1625 UT on day 151 to ≈ 0244 UT on day 153, from ≈ 1546 UT on day 198 to ≈ 0421 UT on day 200, and from ≈ 1622 UT on day 341 to ≈ 0824 UT on day 342. These are shown by light-gray shadings, and marked as CIR_{151}, CIR_{198} and CIR_{341}, respectively according to their starting days. At the CIR leading edges, an abrupt increase in V_{sw} is accompanied by increases in N_{sw}, T_{sw} and B_0. On the other hand, the CIR trailing edges are marked by an increase in

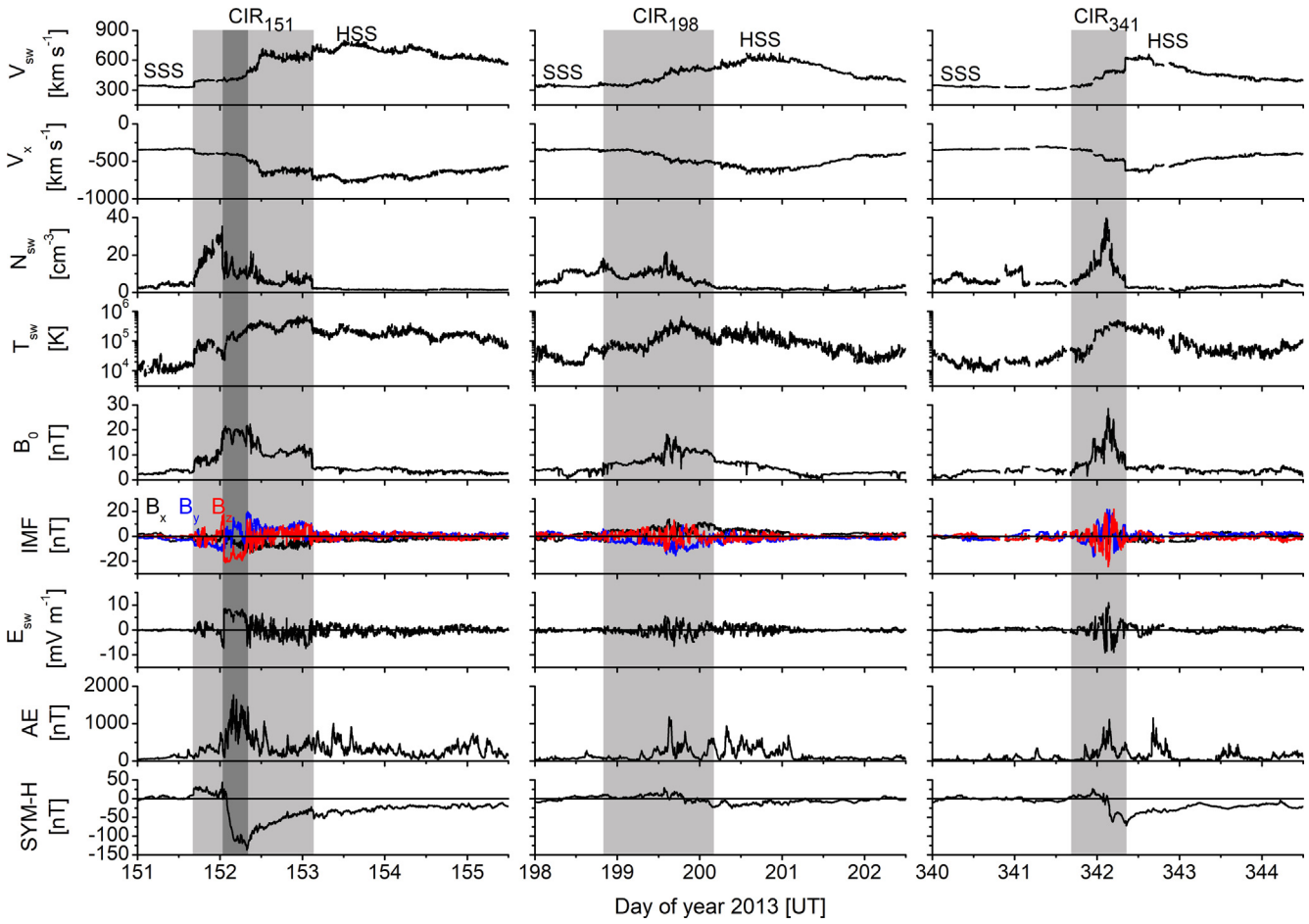

Fig. 1. Three CIRs during 2013. From top to bottom, the panels show solar-wind plasma speed [V_{sw}], plasma velocity radial component [V_x], plasma density [N_{sw}], temperature [T_{sw}], IMF magnitude [B_0], IMF components B_x, B_y, B_z, electric field [E_{sw}], geomagnetic indices AE, and SYM-H, respectively. Light-gray shadings mark the CIR intervals, dark-gray shading in the left panel shows an ICME interval. From left to right, the panels correspond to a CIR-ICME interaction causing an intense storm, a non-geoeffective CIR, and a CIR causing a moderate storm, respectively.

V_{sw}, and decreases in N_{sw}, T_{sw} and B_0. The discontinuities at the CIR boundaries represent potential fast forward and reverse shocks, respectively. However, detailed shock analysis is beyond scope of this study. Interestingly, inside CIR_{151}, a region with smooth and slowly changing IMF components can be noted from ≈ 0037 to 0755 UT on day 152 (marked by a dark-gray shading). This probably represents a small-scale magnetic flux rope or magnetic cloud (MC) interval that is a part of the interplanetary coronal mass ejection (ICME) (Burlaga et al., 1981; Zurbuchen and Richardson, 2006; Cartwright and Moldwin, 2010; Hu et al., 2018). Thus, the first event represents a CIR-ICME interaction event.

The geomagnetic condition is explored by the geomagnetic AE and SYM-H indices. During CIR_{151}, the maximum AE value is 1767 nT at ≈ 0357 UT, and the minimum SYM-H value is −137 nT at ≈ 0748 UT on day 152. The SYM-H value represents an intense storm (see Gonzalez et al., 1994, for classification of storms based on the ring current intensity). During CIR_{198}, the maximum AE (1180 nT) and the minimum SYM-H (−13 nT) values indicate that the CIR was non-geoeffective. CIR_{341} is characterized by a maximum AE of 1116 nT at ≈ 0335 UT and a minimum SYM-H of −72 nT (moderate storm) at ≈ 0830 UT on day 342. Thus, both CIR_{151} and CIR_{341} are geoeffective; they caused an intense storm and a moderate storm, respectively. From this analysis, it is also concluded that the CIR-ICME interaction event (CIR_{151}) is more geoeffective than a "pure" CIR (CIR_{341}). This is consistent with Chi et al. (2018) showing that several CIRs with intense geomagnetic storms are caused by CIR-ICME interaction.

From the analysis of the solar-wind and interplanetary parameters, characteristics of the three CIRs can be compared. The geoeffective events CIR_{151} and CIR_{341} (the non-geoeffective event CIR_{198}) are characterized by the mean V_{sw} values of 658 km s^{-1} and 496 km s^{-1} (465 km s^{-1}), the peak N_{sw} of 35.5 cm^{-3} and 40.0 cm^{-3} (21.1 cm^{-3}), T_{sw} of 7.3×10^5 K and 4.9×10^5 K (6.7×10^5 K), and IMF B_0 of 22.3 nT and 24.7 nT (18.3 nT), respectively. All these parameters (except T_{sw}) have higher values for the geoeffective CIRs than the non-geoeffective event. The most prominent difference is recorded in the IMF B_z-component. While B_z is strongly fluctuating during all of

the events, the geoeffective event CIR_{151} is characterized by a long-duration (6.6 hours) southward IMF with a minimum B_z of −21.2 nT. This is in fact a part of the CIR-ICME interaction. The other geoeffective event CIR_{341} had several long-duration southward IMF components, two prominent intervals of 1.8 and 1.4 hours had the peak B_z intensities of −15.2 and −24.3 nT, respectively. On the other hand, the non-geoeffective event CIR_{198} is characterized by short-duration southward IMF components with the minimum B_z of only −11.3 nT. Consistent to these values are the peak VB_s values during the CIR events, namely 8.7 mV s^{-1} (geoeffective CIR_{151}), 5.6 mV s^{-1} (non-effective CIR_{198}) and 11.0 mV s^{-1} (geoeffective CIR_{341}).

3.2. Statistical results

To summarize the case studies shown in Fig. 1, all the solar-wind parameters are stronger during the geoeffective CIRs than the non-geoeffective CIR. To study the statistical significance of this result, we separated all 290 CIRs (identified by Hajra and Sunny (2022) during 2008–2019) into two groups: geoeffective CIRs causing geomagnetic storms with the SYM-H minimum $\leqslant -50$ nT, and non-geoeffective CIRs with the minimum SYM-H > -50 nT. Among the 290 events, 88 (30%) are found to be geoeffective and 202 (70%) are non-geoeffective. It can be noted that if low-resolution (one-hour) geomagnetic index Dst was used (instead of SYM-H) to identify and classify the geomagnetic storms (with criterion: Dst $\leqslant -50$ nT), the CIR geoeffectiveness reduces to ≈ 25%. This is because the Dst index, due to its low resolution, misses few moderate intensity geomagnetic storms. On the other hand, it is possible for some events which had most of time Dst > -50 nT and to be a weak storm only to have 1 or 2 points with spikes to −50 nT in the one-minute SYMH data. However, use of the high-resolution SYM-H index is preferable or recommended to study geomagnetic activity.

Fig. 2 shows distributions of the CIR characteristic parameters and the peak geomagnetic indices separately during all geoeffective and non-geoeffective CIRs. Based on these distributions, the statistical median, mean and standard deviations are estimated, and listed in Table 1. The ranges of the parameters, from the minimum to the maximum values for all events, are also listed. Significance of the statistics is verified by computation of two-tailed p-values using the median values of the parameters and number of the events, based on the Wilcoxon Rank Sum Test (Gibbons and Chakraborti, 2011). This test is a nonparametric test for two samples with any distribution type (normal or not). If the p-value is less than 0.05 for a distribution, the conclusion is that the two parameters are significantly different from each other (Press et al., 1992).

From the distributions (Fig. 2), all the parameters are found to exhibit large variations from one event to the other. This is confirmed by large ranges of the parameters, and significantly high standard deviations, ≈ 13–68% of the mean values (Table 1).

On average, geoeffective and non-geoeffective CIRs have almost identical duration (≈ 28 and 26 hours, respectively), radial extent (≈ 0.33 and 0.30 AU, respectively), and mean plasma V_{sw} (≈ 503 and 491 km s^{-1}, respectively). It can be noted that the maximum V_{sw} reached by the geoeffective and non-geoeffective CIRs are 647 and 719 km s^{-1}, respectively. As expected, the corresponding p-values are greater than 0.05, indicating that the characteristic parameters are not significantly different for geoeffective and non-geoeffective events.

The solar-wind plasma and IMF compressions are found to be significantly stronger during the geoeffective CIRs than the non-geoeffective events (Table 1). This is confirmed by p-values less than 0.05. On average, the geoeffective CIRs have ≈ 25% higher N_{sw}, ≈ 45% higher P_{sw}, ≈ 42% higher T_{sw}, ≈ 39% higher IMF B_0, ≈ 57% stronger B_s, and ≈ 61% stronger VB_s than the non-geoeffective events.

As a consequence, the auroral electrojet index AE and the ring current index SYM-H are found to be, respectively, ≈ 58% and ≈ 192% higher during the geoeffective CIRs than the non-geoeffective events, on average. The average SYM-H (-78 ± 32 nT) and AE (1523 ± 411 nT) for all geoeffective CIRs indicate moderate geomagnetic activity (Gonzalez et al., 1994).

The quantitative CIR characteristic parameters presented in Fig. 2 and Table 1 can be compared with previously reported results. Alves et al. (2006) studied the CIR characteristics using solar-wind measurements shifted to the Earth's bow-shock nose during 1964–2003. Based on the study of 272 CIRs during this period, Alves et al. (2006) reported an average (median) B_0 value of 13.5 ± 4.2 nT (13.0 nT), and an average (median) negative B_z of -7.0 ± 3.1 nT (−6.5 nT) for all events, including geoeffective and non-geoeffective CIRs. The values are comparable with those for the non-geoeffective events, and weaker than those for the geoeffective events computed in the present work.

Based on a study of 365 CIRs encountered by the *Advanced Composition Explorer* (ACE) and *Wind* spacecraft during 1995–2004, Jian et al. (2006) reported an average B_0 of 15.5 ± 0.26 nT. This is greater than the mean B_0 for the non-geoeffective events and less than the same for the geoeffective events computed in the present work. Their estimated mean duration (36.7 ± 0.9 hours) and radial extent (0.41 ± 0.01 AU) are significantly larger than both geoeffective and non-geoeffective events in the present work. Hajra and Sunny (2022) suggested that this inconsistency might be related to deformation of CIR structures in the OMNI data due to time-shifting process from the spacecraft location to the Earth's bow-shock nose (present work) compared to the original CIR stuctures encountered by the spacecraft (Jian et al., 2006). Another possibility could be any uncertainty in determining the CIR boundaries.

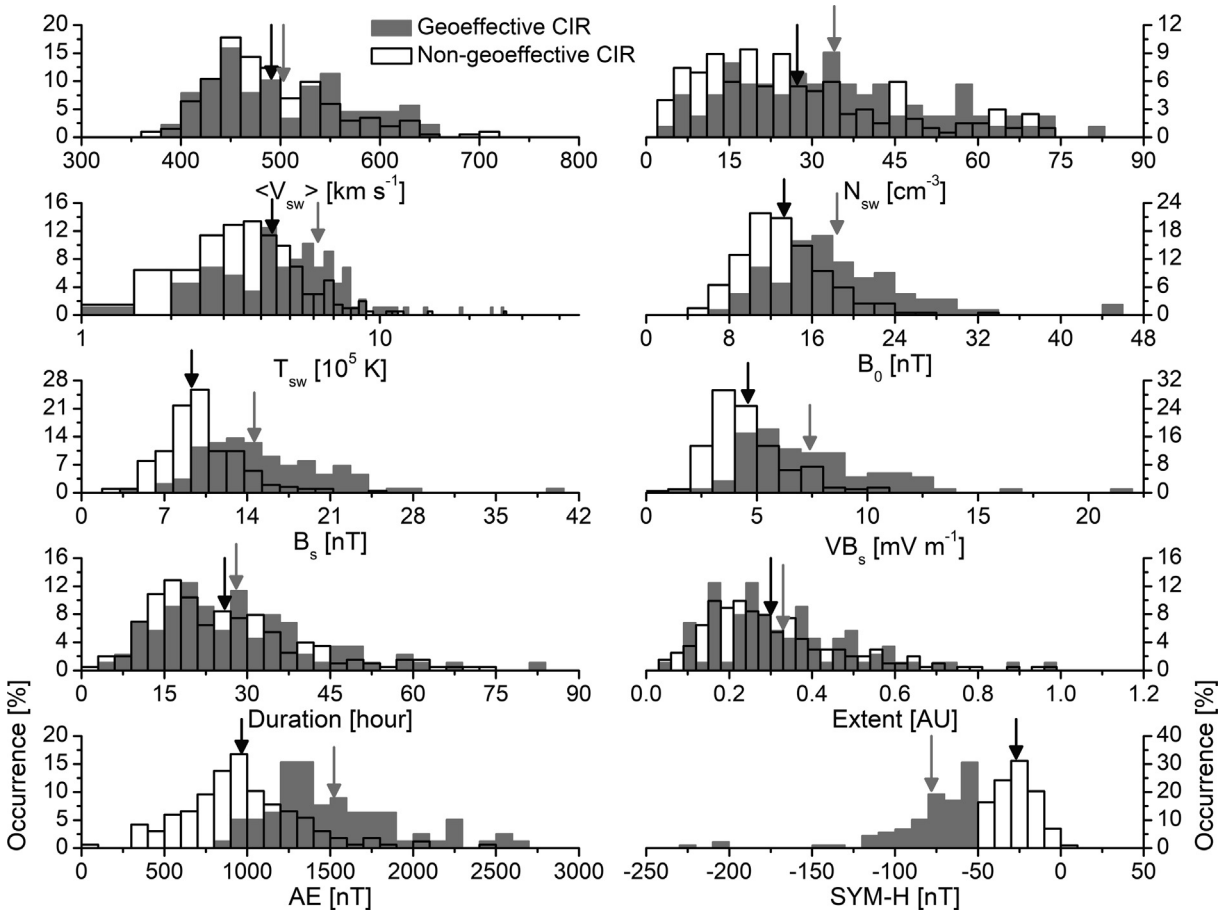

Fig. 2. Histograms of mean V_{sw}, maximum N_{sw}, T_{sw}, B_0, B_z, and VB_s during geoeffective and non-geoeffective CIRs, their duration, and radial extent, maximum AE and minimum SYM-H during geoeffective and non-geoeffective CIRs. Gray and empty histograms correspond to geoeffective and non-geoeffective CIRs, respectively. Downward arrows indicate mean values of the parameters for all geoeffective (gray) and non-geoeffective (black) CIRs.

Table 1
Statistical characteristics and geomagnetic activity during geoeffective and non-geoeffective CIRs.

	Geoeffective CIRs			Non-geoeffective CIRs			*p*-value
Parameter	Range[a]	Median	Mean ± σ[b]	Range[a]	Median	Mean ± σ[b]	
$< V_{sw} >$ [km s^{-1}]	[385, 647]	491	503 ± 70	[377, 719]	478	491 ± 63	0.1704
N_{sw} [cm^{-3}]	[4.5, 81.0]	32.5	34.0 ± 18.1	[2.4, 71.9]	23.7	27.3 ± 17.7	0.001584
P_{sw} [nPa]	[3.1, 57.2]	11.3	13.3 ± 9.0	[1.4, 33.6]	8.4	9.2 ± 5.0	< 0.0001
T_{sw} [10^5 K]	[1.00, 25.78]	5.54	6.20 ± 3.93	[0.97, 26.35]	3.84	4.36 ± 2.54	< 0.0001
B_0 [nT]	[6.6, 44.9]	17.2	18.4 ± 6.7	[4.6, 33.4]	12.8	13.3 ± 4.3	< 0.0001
B_s [nT]	[4.0, 38.7]	13.7	14.6 ± 5.5	[1.8, 24.0]	8.7	9.3 ± 3.3	< 0.0001
VB_s [mV m^{-1}]	[1.8, 21.3]	6.6	7.4 ± 3.1	[0.8, 10.5]	4.1	4.6 ± 1.8	< 0.0001
Duration [hours]	[5.25, 82.10]	25.85	28.00 ± 14.65	[2.75, 73.75]	23.05	25.93 ± 13.86	0.2342
Radial Extent [AU]	[0.06, 0.95]	0.29	0.33 ± 0.17	[0.03, 0.96]	0.26	0.30 ± 0.17	0.1093
AE [nT]	[861, 2698]	1409	1523 ± 411	[57, 2451]	926	966 ± 355	< 0.0001
SYM-H [nT]	[−38.7, −4.0]	−71	−78 ± 32	[−49, 1]	−26	−27 ± 12	< 0.0001

[a] Range: [Minimum, Maximum].
[b] σ: Standard deviation.

Jian et al. (2019) explored 575 CIRs encountered by the *Solar Terrestrial Relations Observatory* (STEREO) spacecraft during 2007–2016. Accordingly, the CIRs during Solar Cycle 24 are characterized by a mean (median) P_{sw} of 7.3 ± 0.2 nPa (6.0 nPa), and a mean (median) B_0 of 13.3 ± 0.2 nT (12.5 nT). Both the B_0 and P_{sw} values are comparable to those of the non-geoeffective events, and less than the geoeffective events under the present work.

4. Conclusions

As mentioned before, a large volume of works has been reported on the CIR variations with the solar cycle, the solar-wind and interplanetary characteristics of the CIRs, and their impacts on the magnetosphere-ionosphere-ther mosphere system. Recently Hajra and Sunny (2022) explored all CIR events encountered by Earth during the recently complete Solar Cycle 24, and compared their results with earlier reported results. However, one important question remains. Can the geoeffective CIRs (causing geomagnetic storms with SYM-H minimum $\leqslant -50$ nT) be distinguished from the non-geoeffective CIRs? To our knowledge, this question was never addressed before. Our study reveals that the answer is yes. Based on a robust statistical study, it is found that geoeffective events are characterized by statistically significant higher plasma density, ram pressure, temperature, IMF intensity, stronger IMF southward component B_s, and stronger reconnection electric field VB_s than the non-geoeffective events.

Geoeffectiveness of a space weather event is mainly controlled by the southward IMFs that reconnect with the (northward) geomagnetic fields leading to enhanced energy coupling between the solar wind and the terrestrial magnetosphere (Dungey, 1961; Gonzalez et al., 1994). This scenario is supported by stronger IMF B_s and VB_s during the geoeffective CIRs. In addition to this, enhanced plasma density and ram pressure seem to strengthen the coupling. However, the mean plasma speed during the CIRs, and the CIR duration and radial extent do not exhibit any significant differences between the geoeffective and non-geoeffective events.

We provide typical values (median and mean) of the characteristic solar and interplanetary parameters, and geomagnetic indices for geoeffective and non-geoeffective CIRs. These can be useful for modeling as well as prediction of CIRs and their geoeffectiveness.

Declaration of Competing Interest

The authors declare that they have no known competing financial interests or personal relationships that could have appeared to influence the work reported in this paper.

Acknowledgments

The work of R. Hajra is funded by the Science and Engineering Research Board (SERB, Grant No. SB/S2/RJN-080/2018), a statutory body of the Department of Science and Technology (DST), Government of India through the Ramanujan Fellowship. The solar-wind plasma and magnetic field data are collected from NASA's OMNIWeb (https://omniweb.gsfc.nasa.gov/). The geomagnetic indices are obtained from the World Data Center for Geomagnetism, Kyoto, Japan (https://wdc.kugi.kyoto-u.ac.jp/). The CIR event list is obtained from the Electronic Supplementary Material available at https://doi.org/10.1007/s11207-022-01962-1. R. Hajra thanks Bruce T. Tsurutani for the helpful scientific discussions. We would like to thank the reviewers for extremely valuable suggestions that substantially improved the manuscript.

References

Alves, M., Echer, E., Gonzalez, W., 2011. Geoeffectiveness of solar wind interplanetary magnetic structures. J. Atmos. Solar Terr. Phys. 73, 1380–1384. https://doi.org/10.1016/j.jastp.2010.07.024.

Alves, M.V., Echer, E., Gonzalez, W.D., 2006. Geoeffectiveness of corotating interaction regions as measured by Dst index. J. Geophys. Res. 111, A07S05. https://doi.org/10.1029/2005JA011379.

Belcher, J.W., Davis Jr., L., 1971. Large-amplitude Alfvén waves in the interplanetary medium, 2. J. Geophys. Res. 76, 3534–3563. https://doi.org/10.1029/JA076i016p03534.

Burlaga, L., Sittler, E., Mariani, F., et al., 1981. Magnetic loop behind an interplanetary shock: Voyager, helios, and imp 8 observations. J. Geophys. Res. 86, 6673–6684. https://doi.org/10.1029/JA086iA08p06673.

Burton, R.K., McPherron, R.L., Russell, C.T., 1975. An empirical relationship between interplanetary conditions and dst. J. Geophys. Res. 80, 4204–4214. https://doi.org/10.1029/JA080i031p04204.

Cannon, P., Angling, M., Barclay, L. et al., 2013. Extreme Space Weather: Impacts on Engineered Systems and Infrastructure. Technical Report Royal Academy of Engineering, Prince Philip House, 3 Carlton House Terrace, London SW1Y 5DG. URL: www.raeng.org.uk/spaceweather.

Cartwright, M.L., Moldwin, M.B., 2010. Heliospheric evolution of solar wind small-scale magnetic flux ropes. J. Geophys. Res. 115, A08102. https://doi.org/10.1029/2009JA014271.

Chapman, S., Bartels, J., 1940. Geomagnetism volume 1 of bb. Oxford University Press, Oxford.

Chi, Y., Shen, C., Luo, B., et al., 2018. Geoeffectiveness of stream interaction regions from 1995 to 2016. Space Weather 16, 1960–1971. https://doi.org/10.1029/2018SW001894.

Daglis, I.A., Thorne, R.M., Baumjohann, W., et al., 1999. The terrestrial ring current: Origin, formation, and decay. Rev. Geophys. 37, 407–438. https://doi.org/10.1029/1999RG900009.

Davis, T.N., Sugiura, M., 1966. Auroral electrojet activity index AE and its universal time variations. J. Geophys. Res. 71, 785–801. https://doi.org/10.1029/JZ071i003p00785.

Dungey, J.W., 1961. Interplanetary magnetic field and the auroral zones. Phys. Rev. Lett. 6, 47–48. https://doi.org/10.1103/PhysRevLett.6.47.

Echer, E., Gonzalez, W.D., Guarnieri, F.L., et al., 2005. Introduction to space weather. Adv. Space Res. 35, 855–865. https://doi.org/10.1016/j.asr.2005.02.098.

Finch, I.D., Lockwood, M.L., Rouillard, A.P., 2008. Effects of solar wind magnetosphere coupling recorded at different geomagnetic latitudes: Separation of directly-driven and storage/release systems. Geophys. Res. Lett. 35, L21105. https://doi.org/10.1029/2008GL035399.

Franco, A.M.S., Hajra, R., Echer, E., et al., 2021. Seasonal features of geomagnetic activity: a study on the solar activity dependence. Ann. Geophys. 39, 929–943. https://doi.org/10.5194/angeo-39-929-2021.

Frank, L.A., 1967. On the extraterrestrial ring current during geomagnetic storms. J. Geophys. Res. 72, 3753–3767. https://doi.org/10.1029/JZ072i015p03753.

Gardner, L., Sojka, J.J., Schunk, R.W., et al., 2012. Changes in thermospheric temperature induced by high-speed solar wind streams. J. Geophys. Res. 117, A12303. https://doi.org/10.1029/2012JA017892.

Gibbons, J.D., Chakraborti, S., 2011. Nonparametric statistical inference. In: International Encyclopedia of Statistical Science. Springer, Berlin Heidelberg, Berlin, Heidelberg, pp. 977–979. https://doi.org/10.1007/978-3-642-04898-2_420.

Gonzalez, W.D., Joselyn, J.A., Kamide, Y., et al., 1994. What is a geomagnetic storm?. J. Geophys. Res. 99 5771–5792. https://doi.org/10.1029/93JA02867.

Hajra, R., 2021. September 2017 space-weather events: A study on magnetic reconnection and geoeffectiveness. Solar Phys. 296, 50. https://doi.org/10.1007/s11207-021-01803-7.

Hajra, R., 2022a. Intense geomagnetically induced currents (GICs): Association with solar and geomagnetic activities. Solar Phys. 297, 14. https://doi.org/10.1007/s11207-021-01945-8.

Hajra, R., 2022b. Intense, long-duration geomagnetically induced currents (GICs) caused by intense substorm clusters. Space. Weather 20. https://doi.org/10.1029/2021SW002937, e2021SW002937.

Hajra, R., Echer, E., Tsurutani, B.T., et al., 2013. Solar cycle dependence of high-intensity long-duration continuous AE activity (HILDCAA) events, relativistic electron predictors? J. Geophys. Res. 118, 5626–5638. https://doi.org/10.1002/jgra.50530.

Hajra, R., Henri, P., Myllys, M., et al., 2018. Cometary plasma response to interplanetary corotating interaction regions during 2016 June–September: a quantitative study by the Rosetta Plasma Consortium. Mon. Not. Roy. Astron. Soc. 480, 4544–4556. https://doi.org/10.1093/mnras/sty2166.

Hajra, R., de Souza, Marques, Franco, A., Echer, E., et al., 2021. Long-term variations of the geomagnetic activity: A comparison between the strong and weak solar activity cycles and implications for the space climate. J. Geophys. Res. 126. https://doi.org/10.1029/2020JA028695, e2020JA028695.

Hajra, R., Sunny, J.V., 2022. Corotating interaction regions during solar cycle 24: A study on characteristics and geoeffectiveness. Solar Phys. 297, 30. https://doi.org/10.1007/s11207-022-01962-1.

Hajra, R., Sunny, J.V., Babu, M., et al., 2022. Interplanetary sheaths and corotating interaction regions: A comparative statistical study on their characteristics and geoeffectiveness. Solar Phys. 297, 97. https://doi.org/10.1007/s11207-022-02020-6.

Hajra, R., Tsurutani, B.T., 2018. Chapter 14 - magnetospheric "killer" relativistic electron dropouts (REDs) and repopulation: A cyclical process. In: Buzulukova, N. (Ed.), Extreme Events in Geospace. Elsevier, Amsterdam, pp. 373–400. https://doi.org/10.1016/B978-0-12-812700-1.00014-5.

Hajra, R., Tsurutani, B.T., Brum, C.G.M., et al., 2017. High-speed solar wind stream effects on the topside ionosphere over arecibo: A case study during solar minimum. Geophys. Res. Lett. 44, 7607–7617. https://doi.org/10.1002/2017GL073805.

Hajra, R., Tsurutani, B.T., Lakhina, G.S., 2020. The complex space weather events of 2017 September. Astrophys. J. 899, 3. https://doi.org/10.3847/1538-4357/aba2c5.

Hu, Q., Zheng, J., Chen, Y., et al., 2018. Automated detection of small-scale magnetic flux ropes in the solar wind: First results from the Wind spacecraft measurements. Astrophys. J. Suppl. Ser. 239, 12. https://doi.org/10.3847/1538-4365/aae57d.

Iyemori, T., Takeda, M., Nose, M. et al., 2010. Mid-latitude geomagnetic indices ASY and SYM for 2009 (provisional). URL: wdc.kugi.kyoto-u.ac.jp/aeasy/asy.pdf.

Jian, L., Russell, C.T., Luhmann, J.G., et al., 2006. Properties of stream interactions at one au during 1995–2004. Solar Phys. 239, 337–392. https://doi.org/10.1007/s11207-006-0132-3.

Jian, L.K., Luhmann, J.G., Russell, C.T., et al., 2019. Solar terrestrial relations observatory (STEREO) observations of stream interaction regions in 2007–2016: Relationship with heliospheric current sheets, solar cycle variations, and dual observations. Solar Phys. 294, 31. https://doi.org/10.1007/s11207-019-1416-8.

Lakhina, G.S., Hajra, R., Tsurutani, B.T., 2020. Geomagnetically induced currents. In: Gupta, H.K. (Ed.), Encyclopedia of Solid Earth Geophysics. Springer International Publishing, Cham, pp. 1–4. https://doi.org/10.1007/978-3-030-10475-7_245-1.

Lei, J., Thayer, J.P., Wang, W., et al., 2011. Impact of CIR storms on thermosphere density variability during the solar minimum of 2008. Solar Phys. 274, 427–437. https://doi.org/10.1007/s11207-010-9563-y.

Pizzo, V., 1978. A three-dimensional model of corotating streams in the solar wind, 1. theoretical foundations. J. Geophys. Res. 83, 5563–5572. https://doi.org/10.1029/JA083iA12p05563.

Press, W.H., Teukolsky, S.A., Vetterling, W.T., et al., 1992. Numerical recipes in c: The art of scientific computing, 2nd ed. Cambridge University Press.

Richardson, I.G., Cliver, E.W., Cane, H.V., 2000. Sources of geomagnetic activity over the solar cycle: Relative importance of coronal mass ejections, high-speed streams, and slow solar wind. J. Geophys. Res. 105, 18203–18213. https://doi.org/10.1029/1999JA000400.

Siscoe, G.L., 1972. Structure and orientations of solar-wind interaction fronts: Pioneer 6. J. Geophys. Res. 77, 27–34. https://doi.org/10.1029/JA077i001p00027.

Smith, E.J., Wolfe, J.H., 1976. Observations of interaction regions and corotating shocks between one and five AU: Pioneers 10 and 11. Geophys. Res. Lett. 3, 137–140. https://doi.org/10.1029/GL003i003p00137.

Tsurutani, B.T., Gonzalez, W.D., 1987. The cause of high-intensity long-duration continuous ae activity (hildcaas): Interplanetary alfvén wave trains. Planet. Space Sci. 35, 405–412. https://doi.org/10.1016/0032-0633(87)90097-3.

Tsurutani, B.T., Gonzalez, W.D., Gonzalez, A.L.C., et al., 2006. Corotating solar wind streams and recurrent geomagnetic activity: A review. J. Geophys. Res. 111, A07S01. https://doi.org/10.1029/2005JA011273.

Tsurutani, B.T., Gonzalez, W.D., Tang, F., et al., 1992. Great magnetic storms. Geophys. Res. Lett. 19, 73–76. https://doi.org/10.1029/91GL02783.

Tsurutani, B.T., Hajra, R., 2021. The interplanetary and magnetospheric causes of geomagnetically induced currents (GICs) >10 a in the Mäntsälä Finland pipeline: 1999 through 2019. J. Space Weather Space Clim. 11, 23. https://doi.org/10.1051/swsc/2021001.

Tsurutani, B.T., Hajra, R., Echer, E. et al., 2016b. Predicting magnetospheric relativistic > 1 MeV electrons. NASA Tech Briefs, 40, 20. URL: www.techbriefs.com/component/content/article/ntb/tech-briefs/software/24815.

Tsurutani, B.T., Hajra, R., Tanimori, T., et al., 2016a. Heliospheric plasma sheet (HPS) impingement onto the magnetosphere as a cause of relativistic electron dropouts (REDs) via coherent EMIC wave scattering with possible consequences for climate change mechanisms. J. Geophys. Res. 121, 10130–10156. https://doi.org/10.1002/2016JA022499.

Tsurutani, B.T., Ho, C.M., Arballo, J.K., et al., 1995. Large amplitude imf fluctuations in corotating interaction regions: Ulysses at midlatitudes. Geophys. Res. Lett. 22, 3397–3400. https://doi.org/10.1029/95GL03179.

Tsurutani, B.T., Lakhina, G.S., Hajra, R., 2020. The physics of space weather/solar-terrestrial physics (stp): what we know now and what the current and future challenges are. Nonlin. Processes Geophys. 27, 75–119. https://doi.org/10.5194/npg-27-75-2020.

Verbanac, G., Vrsnak, B., Veronig, A., et al., 2011. Equatorial coronal holes, solar wind high-speed streams, and their geoeffectiveness. Astron. Astrophys. 526, A20. https://doi.org/10.1051/0004-6361/201014617.

Wanliss, J.A., Showalter, K.M., 2006. High-resolution global storm index: Dst versus SYM-H. J. Geophys. Res. 111, A02202. https://doi.org/10.1029/2005JA011034.

Williams, D.J., 1987. Ring current and radiation belts. Rev. Geophys. 25, 570–578. https://doi.org/10.1029/RG025i003p00570.

Zhang, Y., Sun, W., Feng, X.S., et al., 2008. Statistical analysis of corotating interaction regions and their geoeffectiveness during solar cycle 23. J. Geophys. Res. 113, A08106. https://doi.org/10.1029/2008JA013095.

Zurbuchen, T.H., Richardson, I.G., 2006. In-situ solar wind and magnetic field signatures of interplanetary coronal mass ejections. Space Sci. Rev. 123, 31–43. https://doi.org/10.1007/s11214-006-9010-4.